Chapter 4

Charge Ordering at a Dielectric Gate in Itinerant Metallic States with Low-Field Memristor Properties in VO_2 Thin Film

4.1 Introduction

In VO_2, the electrical conductivity rises up progressively at thermally induced itinerant metallic VO_2 states. The exotic 'e^--h^+' pairs, which order at thermal induced itinerant energy states of coupled 'e-p' [1, 2], result in a hysteretic loop of the resulting resistivity across the T_c point in a thermal cycle. The energy stored in the loop is a 'figure of merit' of its applications in memristor and other memory devices. A similar effect also emerges at photoexcitation of 'e^--h^+' pairs by applying UV-visible radiations [3–6], electric fields [7–9], or other stimuli [7–10]. Strongly correlated itinerant states (of charge, phonon, orbital, and spin) of the degree of freedom can be explored to tune the 'pertinent signal' in several ways.

In the lattice structure, M_1-VO_2 near RT [3, 4, 11, 12] successively changes, $M_1 \rightarrow M_2 \rightarrow R_1/R_2/R$-$VO_2$, as $T \rightarrow T_c$, or beyond. An interface $M_1 \rightarrow M_2 \rightarrow R_1/R_2/R$-$VO_2$ regulates the exotic charge features. A chemical bonding at the substrate controls VO_2 order along it that regulates dynamics of the 'charge carriers' in conductive channels of a $1 \rightarrow 2D$ network at a nanoscale. In general, the materials are used in devices in three basic forms; bulk, NAs, and thin films. At limited thickness, $t \leq 100$ nm, thin films can order in coherent NAs, $0 \rightarrow 2D$, of small islands (clusters) in an anisotropic texture [6, 13]. The topology in atoms order at the itinerant surface states in the NAs on a substrate (template)

actively tunes the field-dependent properties [9, 14]. These are some of the basic clues in designing and devising quality-controlled films with co-planar NAs in synergetic shapes (nanoplates, nanobeams, nanotubes, or nanowires [15, 16] of variety of materials [13, 16–19]. Exclusively, a memristor (a memory resistor) functions in solid-state electronic and ionic transports are coupled under a bias field [7, 20]. A hysteresis I-V (current-voltage) loop is observed in nanoscale memristors [7, 13, 16–20] in field-induced motion of exotic 'charge carriers' in inorganic/organic solid-state electronics [9, 17–20].

For example, an electro-optic modulator of VO_2@Si films efficiently probes the $M_1 \rightarrow$ R-VO_2 transition forth and back in a reversible cycle [21]. An order of induced 'I' is peaked up at a threshold field (V_t) ~ 1.7 V, but no significant $M_1 \leftrightarrow$ R-VO_2 hysteresis persists. More recently, Yu et al. studied $M_1 \leftrightarrow$ R-VO_2 switching at VO_2/SiO_2/Si films (t ~ 300 nm), having big crystallites, $D_c \geq 80$ nm size, which are not so easy to keep (011) uniaxial along the films [22]. A W^{6+}-$5d^0$ (DM at $s = 0$) doped VO_2, ≤ 4 wt % W^{6+}, is shown to exhibit an effective way to control $V_t \leq 1$ V [10]. It duly suppresses $T_c \rightarrow 308$ K ± 5 K, suitable for uses near RT. It also promotes conductivity and heat generation (Joule heating effect), which are beneficial to triggering the T_c signal at low fields [10, 23]. At T ~ 297 K, VO_2/TiO_2 extends a wide hysteresis of the resistivity, as well as the I-V loop at low fields, ≤ 3 V [24]. A core VO_2 shell ($t \leq 3$ nm) at SiO_2 in a polymer, such as PVP, is shown to trigger thermal and electro-induced T_c signal (a wide hysteresis) at resistivity suddenly declines at $T \rightarrow T_c$ [25]. Obviously, uniaxial VO_2-NAs are required to duly lower T_c and regulate functionalized properties at field-induced charge carriers.

This chapter focuses on the study of a polymer PVP assisted M_1-VO_2 of thin films, $t \leq$ 100 nm, with a nano SiO_2/TiO_2 gate on a (100) Si(p^{++}) substrate. Both SiO_2 and TiO_2 (as a template) support over a uniaxial (011) VO_2 growth in NCs primarily along the films. The microscopic VO_2 charge ordering is studied with XRD, microscopic images, and

XPS of the pertinent films. A prominent field-induced T_c signal is triggered near RT to make use of these VO_2 films in memristor and other electronic devices. A charge ordering at the itinerant VO_2 metallic states controls the I-V response in correlation to inbuilt NAs and interfaces at the nanogate. A wide I-V hysteresis (reversible) is tailored, especially at (011) VO_2 NCs grown on the TiO_2@Si of 'conducting through channels' of exotic charge carriers.

4.2 Results and Discussion

4.2.1 Tailored Lattice Structure VO_2 at a Buffer Layer

A buffer layer SiO_2/TiO_2 of a well smooth surface is used to coat over VO_2 in a compatible topology of an electronic grade film at a (100) Si(p^{++}) substrate. This is studied with FESEM images of SiO_2/TiO_2 coated separately on the Si(p^{++}) in the identical conditions. As shown in **Figure 4.1 (a to d)**, FESEM images present well smooth and homogenous surfaces down to a few nm scales. The FESEM images at a closer view in **Figure 4.1 (b, d)** reveal ultrafine SiO_2/TiO_2 (5-10 nm sizes) order in tiny 2D clusters. The surface roughness is marginally changed in a limited surface diffusion caused by low thermal energy and a finite-size effect of small species. We studied various films and that all give similar topologies. The precursor and post-anneals are crucial to keep NAs aligned along the films. The thin films VO_2@Si, $t \leq 100$ nm, made with a buffer layer SiO_2/TiO_2 maintain well smooth surfaces at a similar nanoscale. This is shown in the AFM images compared in **Figure 4.2 (a, b, c)**, with a typical 3D image in the right panel. A bit larger roughness, rms $\rightarrow$ 2.0 nm, is reported at random spots of 2μm x 2μm area at these films. As usual, the rms value is shown to vary a little, within ± 20 %, as on scanned at varied regions at the films. A small rms ≤ 2.0 nm confers a high quality of the films. The VO_2 films when grown directly at the Si in **Figure 4.2 (a)** display rather bigger VO_2

plates and few cuboids/bars, with w = 25-50 nm widths and L = 25-75 nm lengths. Well-refined NAs, with w = 15-25 nm at L = 25-50 nm, are shown in **Figure 4.2 (b)** after a SiO_2 buffer is used, while those have w = 15-30 nm at L = 20-50 nm in **Figure 4.2 (c)** after a TiO_2 buffer is used. The XRD patterns in the VO_2 films in **Figure 4.3 (a, b, c)** exhibit only two peaks of the M_1-VO_2 phase are grown uniaxial in the (011) and (022) lattices.

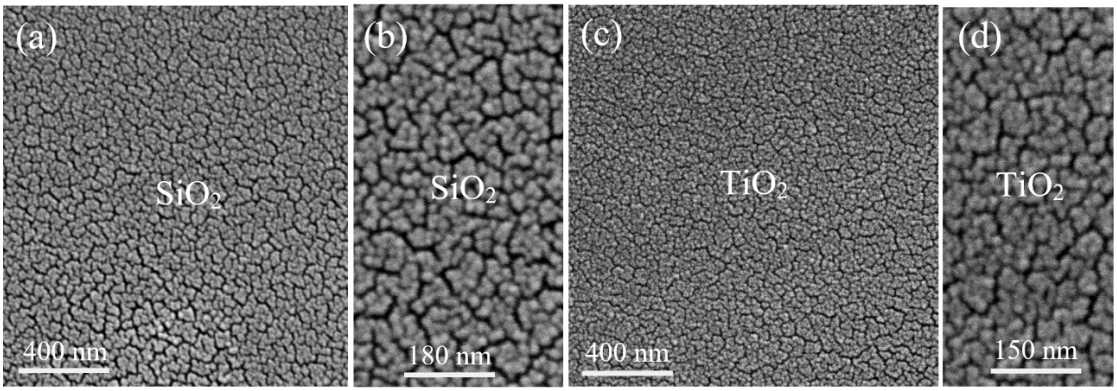

Figure 4.1 (a → d) FESEM images of SiO_2 and TiO_2 thin films on a Si(p^{++}) substrate. Small SiO_2/TiO_2 clusters are visible in magnified (b, d) FESEM images.

No other peak is observed in a range of $2\theta = 10° \rightarrow 90°$, wherein several other peaks arise if VO_2 is not aligned so well along the films [26, 27]. Also, no amorphous phase is visible. It ensures a high degree of VO_2 crystallinity. Otherwise, a broad halo(s) intrinsic of an amorphous (disordered) phase [28] is superposed on a scattering background in this region [5, 29]. Evidently, a bare as well as a coated Si(p^{++}) with a buffer layer SiO_2/TiO_2 bonds over VO_2 well aligned in NCs along the interface. Such a high degree of aligned (011) VO_2 is not known so far [5, 22]. Thin films, t = 20-30 nm, of a sol-gel VO_2 on an n-type (100) Si exhibits (011) and (211) peaks superposed on a broad XRD halo of an amorphous phase [30]. At larger $t \rightarrow$ 300 nm, VO_2 is shown to form in multiple shapes,

which exhibit five more XRD peaks at $2\theta = 25°$ to $60°$ in $V_2O_5 \rightarrow 2VO_2 + ½\ O_2\uparrow$ sputtered at SiO_2/n-Si [22]. ALD-VO_2 films reveal (001) VO_2 NCs at Si, or glasses [31], while a doped $W_xV_{1-x}O_2$, x = 0, 1.27 and 1.59 at %, is grown at (020) planes in magnetron sputtered films, t = 130 nm, at α-Al_2O_3 [23]. Thus, an intimate interface bonding on a substrate and/or a gate of a commensurate network structure is critical to induce, support over (as a template), and regulate the VO_2 grow up aligned at and along it in a non-disrupted process, limited to a critical $t \rightarrow t_c$ scale at the films.

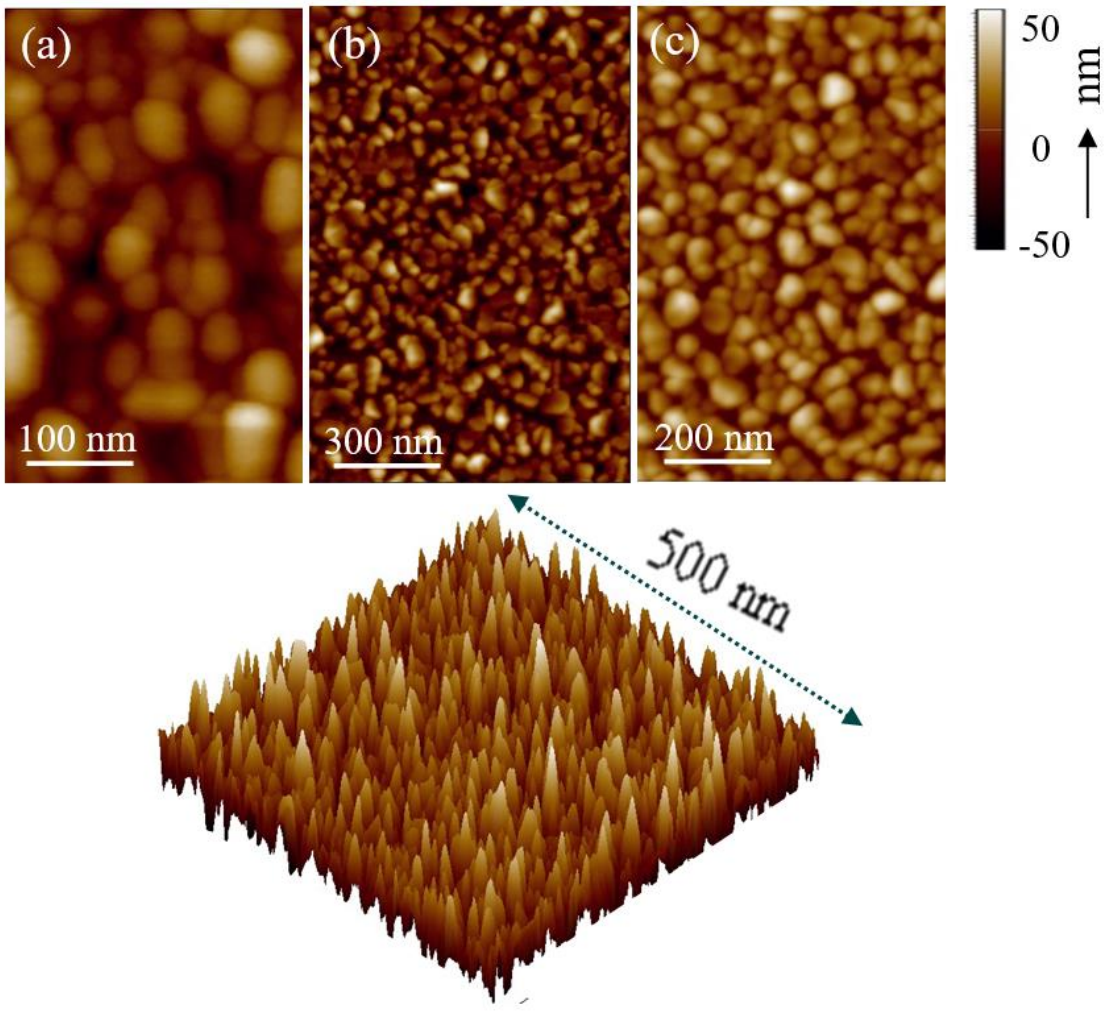

Figure 4.2 AFM images of VO_2 films grown on a Si(p^{++}) substrate (a) before and after using a buffer layer (b) SiO_2 and (c) TiO_2. A 3D image (at bottom) shows (c) a smooth surface (1.8 nm rms).

Thus, an intimate interface bonding on a substrate and/or a gate of a commensurate network structure is critical to induce, support over (as a template), and regulate the VO_2 grow up aligned at and along it in a non-disrupted process, limited to a critical $t \rightarrow t_c$ scale at the films. An interface VO_2 bonding to a commensurate substrate (and/or a gate) used renders and controls the VO_2 lattice strain (γ_c) in the thin films. That is reflected in peak broadening (Δw) in the XRD peaks.

Table 4.1 The XRD peaks in the effects of a SiO_2/TiO_2 gate regulates a uniaxial (011) VO_2 bonding on a (100) Si(p^{++}) substrate in thin films.

d_{hkl} (nm)	h k l	I_p	Δw (10^{-2} nm)	γ_c (%)	Lattice
1. VO_2@Si(p^{++})					
0.3270	0 1 1	100	0.182	1.05	V^{4+}:VO_2
0.1608	0 2 2	07	0.230		V^{4+}:VO_2
2. VO_2@SiO_2/Si(p^{++})					
0.3262	0 1 1	100	0.160	0.75	V^{4+}:VO_2
0.1611	0 2 2	08	0.220		V^{4+}:VO_2
3. VO_2@TiO_2/Si(p^{++})					
0.3275	0 1 1	100	0.475	1.55	V^{4+}:VO_2
0.1612	0 2 2	09	0.250		V^{4+}:VO_2

The I_p and Δw values are accurate within an error bar $\pm$ 10% in the weak and overlapping peaks. Bulk M_1-VO_2; d_{011} = 0.3203 nm and d_{022} = 0.1602 nm [27].

As given in **Table 4.1**, γ_c = 1.05 %, 0.75 %, and 1.55 % is estimated using Δw values in the (011) and (022) XRD peaks (in the Williamson-Hall plot [32]) in the thin VO_2 films on a bare and a coated Si(p^{++}) at a buffer layer of SiO_2 and TiO_2, respectively.

Further, an induced γ_c in the thin VO_2 films is shown up in an induced anharmonicity, $\delta \equiv (d_{011} - 2d_{022}) \leq 1.65$ %, where d_{011}/d_{022} are the interplanar distances in the respective XRD peaks. Otherwise, $\delta \rightarrow 0$ at $D \rightarrow \infty$ at bulk crystals.

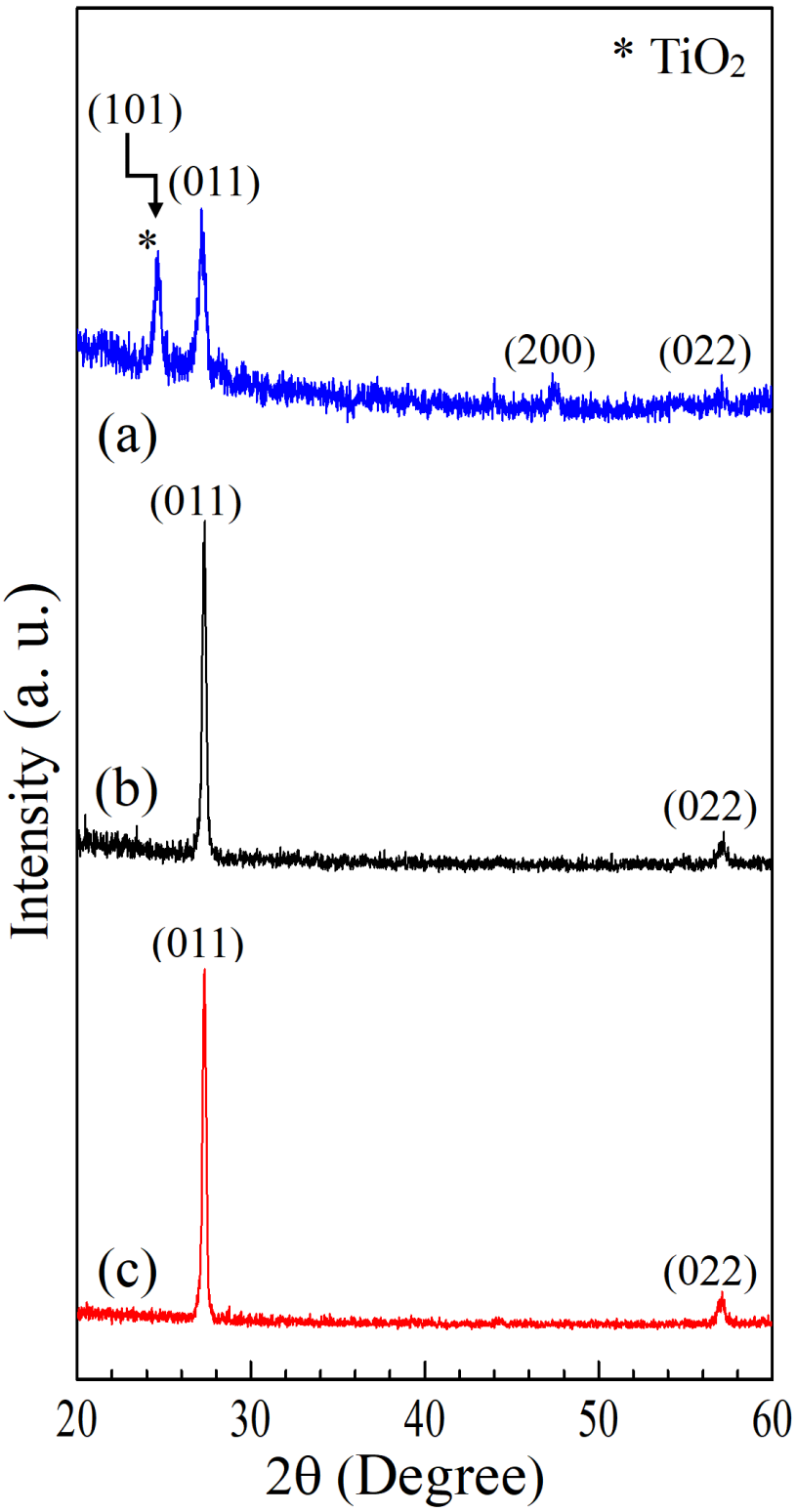

Figure 4.3 XRD patterns of the VO_2 films grown on (a) TiO_2, (b) SiO_2 and (c) Si.

They can be correlated with each other as $\gamma_c = \delta/d_{011}$, which implies γ_c = 1.65 %, 1.23 %, and 1.56 % (at an error bar ≤ 0.05 %) in the respective VO_2 films. An optimized γ_c value seems very useful in order to regulate the low-field memristor devices.

The FESEM images in **Figure 4.4 (a, b, c)** display co-planar VO_2 of nanoplates facing up in (011) facets on the films in small islands. An apparent difference in the three samples is that nanoplates (*w* = 20-40 nm and *L* = 20-80 nm) are bit tilted up at the film surface in **Figure 4.4 (a)** if no buffer is used. A few nanoplates are laid down one over others in a hierarchical structure (cluster), as also shown in the AFM images in **Figure 4.2 (a)**. The nanoplates (aspect ratio $w/L \rightarrow 1$) are rather well separated and uniformly displaced in the films are made using an inbuilt nano-gate SiO_2/TiO_2 at a (100) Si(p^{++}) plate.

A refined pattern contains *w* = 20-50 nm nanoplates in the VO_2@SiO_2-Si films, while those of *w* = 15-30 nm in the VO_2@TiO_2-Si films. Similar FESEM images of nanoplates are also shown in a Ti^{4+}-$3d^0$ doped $V_{1-x}Ti_xO_2$ of spin-coated films at SiO_2 [29], which show up a refined $w = 130 \rightarrow 30$ nm at $x \rightarrow 0.1$ [29]. It is an isoelectronic product of V^{5+}-$3d^0$ doped VO_2 we studied over here in the VO_2@TiO_2-Si films. Thus, a nano-gate n-TiO_2 inbuilt in such films is very effective in refining uniform VO_2 nanoplates.

The results are consistent with the (011) XRD peak width **Table 4.1**, which gives (at Scherrer relation) an average D_c = 20 nm in the VO_2@TiO_2-Si films, 32 nm in the VO_2@Si films, while 30 nm in the VO_2@SiO_2-Si films. $\gamma_c \rightarrow 0.75$ % is relaxed in VO_2 is grown up, $D_c \geq 30$ nm. A close similarity in the D_c and Δw values confirms that the small nanoplates are single NCs. Much bigger polycrystals M_1-VO_2, $D_c \sim 100$ nm, are shown with sharp XRD peaks in rather 300 nm thick films on SiO_2 at an n-Si plate [22].

4.2.2 XPS Bands in Charge Orders via Gate in VO_2 Films

A nanogate in thin films VO_2@Si renders a partial ion-exchange $V^{4+} \rightarrow V^{3+}/V^{5+}$ (also $3d^1 \rightarrow 3d^2/3d^0$ spins) in the $M_1 \rightarrow M_2$-VO_2 metallic states. It is well reflected in XPS bands of the VO_2@TiO_2-Si films as follows.

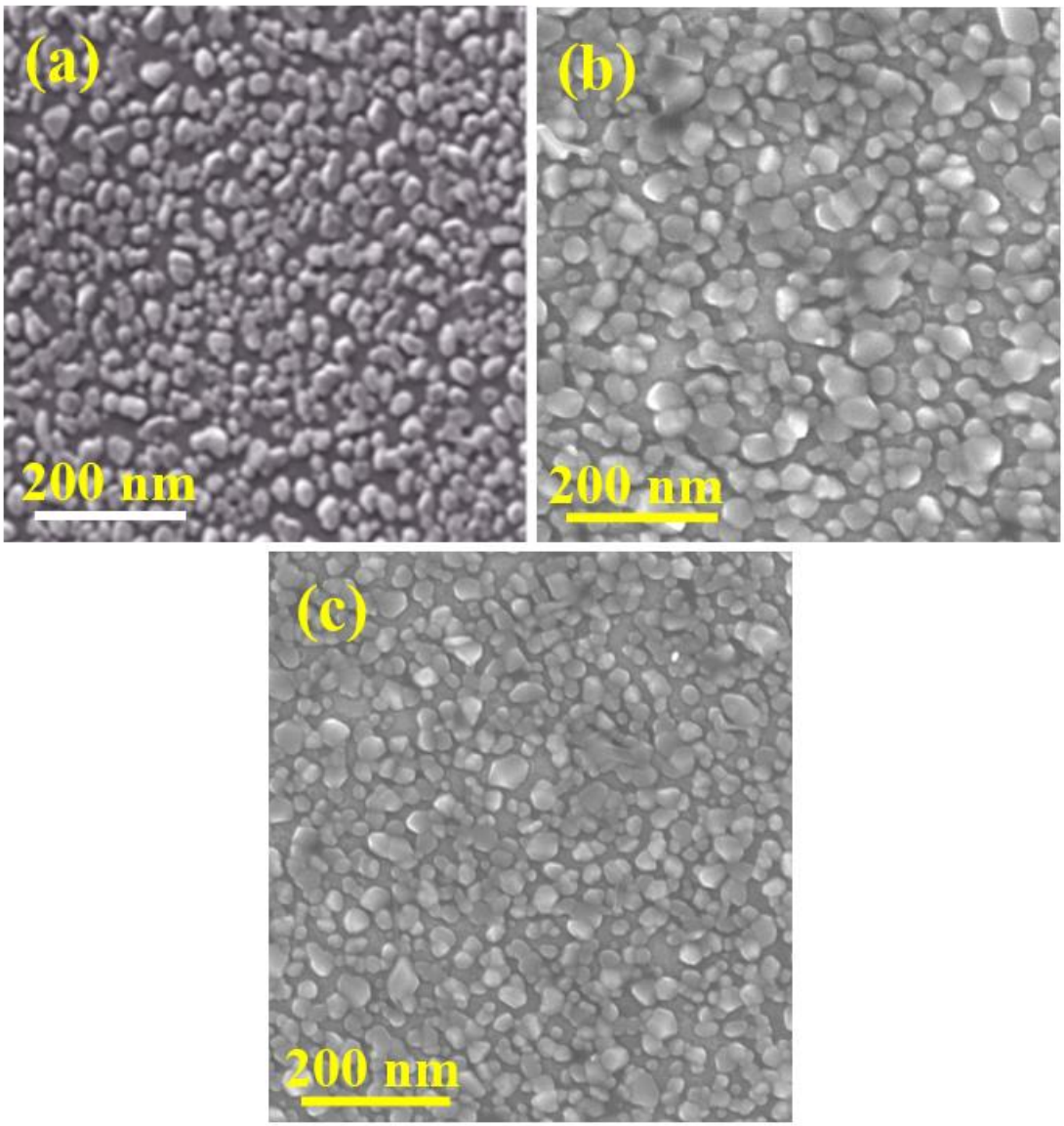

Figure 4.4 FESEM images of the VO_2 films grown on (a) Si, (b) SiO_2 and (c) TiO_2.

Accordingly, the V^{3+}/V^{5+} bands are displaced aside the major V^{4+} bands O-$1s_{1/2}$ and V-$2p_{1/2,3/2}$ in **Figure 4.5 (a to d)** in two major groups over the major V^{4+} bands O-$1s_{1/2}$ and V-$2p_{1/2,3/2}$ in **Figure 4.5 (a to d)** in two major groups over 536 eV-526 eV and 527 eV-512 eV, respectively. The individual bands are marked at bars (at bottom) in the bar heights represent the band intensities.

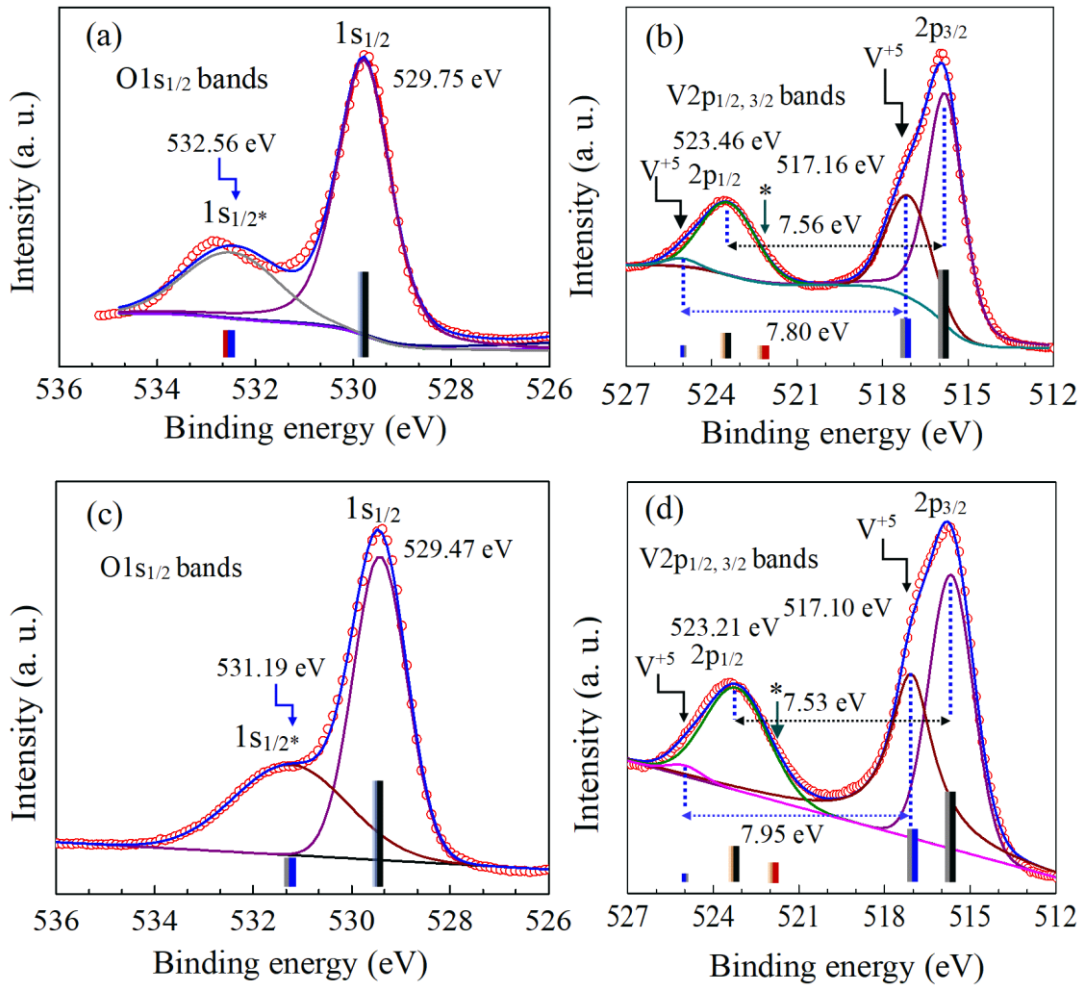

Figure 4.5 The XPS bands O$1s_{1/2}$ and V$2p_{1/2,3/2}$ in thin films VO_2 grown at (a, b) bare and (c, d) TiO_2 coated Si, respectively.

The binding energies (E_b), normalized peak intensities (I_p) at a 0-100 scale, and bandwidths (Δw) for the individual bands are given in **Table 4.2**. Namely, the O^{2-} species

give two deconvoluted bands $1s_{1/2}$ and $1s_{1/2*}$ at E_b = 529.75 eV and 532.56 eV (separation Δs = 2.81 eV) in **Figure 4.5 (a)** in the VO_2@Si films. They belong to two different types O^{2-} moieties formed at V^{4+} and V^{5+} states, respectively, in a network. Upon a nanogate TiO_2 is inbuilt, lowered E_b = 529.47 eV and 531.19 eV (Δs = 1.72 eV) are revived in **Figure 4.5 (c)**, in which the $1s_{1/2*}$ band intensity is merely decreased 31 → 29 % in the O^{2-}-V^{5+} bonds in a 'VO_6^{7-}' type oligomer. A roughly 23 % 'V^{5+}-O^{2-}' is estimated, assuming it is proportional to the $1s_{1/2*}$ band intensity (V^{5+} phase).

Eventually, a reasonably smaller E_b value from a bulk VO_2 of two O-$1s_{1/2}$ bands at 529.88 eV and 531.80 eV (Δs = 2.08 eV) [25] signifies a due effect of an ion exchange 'V^{4+} → V^{5+} + e^-' in the 'conductive network channels' formed in the films. In earlier studies [25, 33], the additional XPS band was assigned to oxygen as free hydroxyl (OH), or water. Such species if co-present gets desorbed off in the XPS measurement is done in high vacuum. Obviously, it is characterising an O^{2-} rich oligomer at charge neutrality at V^{5+} doped M_2-VO_2 states.

A doublet $2p_{1/2,3/2}$ at $3d^1$-V^{4+} in the M_1-VO_2 phase in **Figure 4.5 (b)** is split up into two bands of E_b = 523.46 eV and 515.90 eV, with a crystal field splitting ΔE_b = 7.56 eV, in the VO_2@Si films. In a thin film VO_2@n-Si of an optical memory, bit larger E_b → 523.70 eV and 516.10 eV are reported at ΔE_b = 7.60 eV [34], likely at a charge order, Si^- ← V^{4+}–e^- → V^{5+}, at the interfaces. It is an analogue of a $3d^0$-V^{5+} doped VO_2 we studied here. Thus, the V^{5+} bands reveal further larger E_b = 524.96 eV and 517.16 eV at a wider ΔE_b = 7.80 eV at a revived electronic state $1S^0$ (net spin S = 0) of a DM insulator. As per I_p values in these bands, a roughly 33 % V^{4+} → V^{5+} is transferred, likely at the NCs surfaces in a core-shell type structure [35]. When a n-TiO_2 nanogate is used, the $2p_{1/2,3/2}$ bands are further shifted, ≤ 0.45 eV, at lowered E_b in **Figure 4.5 (d)** at both types V^{4+} → V^{5+} + e^- charges co-exist at the itinerant M_1 → M_2-VO_2 metallic states.

As given in **Table 4.2**, an enhanced $\Delta E_b \rightarrow 7.95$ eV reveals that the crystal field is duly enhanced in an intertwined V^{5+}: M_2-VO_2 lattice (strained). It is a nontrivial parameter to design, control, and monitor field induced switching in the optical/memristor devices [31, 34]. Further, no separate XPS band is visible in $V^{4+} \rightarrow V^{3+}$ species. Possibly, it is reflected in an asymmetry (marked at an arrow) in the $2p_{1/2}$ band, which is shifted 522.15 eV → 521.85 eV on an inbuilt nanogate n-TiO_2 is used. A partial $2V^{4+} \rightarrow V^{3+} + V^{5+}$ charge order on the n-TiO_2 interface (as a catalyst) can interplay a crucial role in duly tuning the profound electronic properties.

Table 4.2 The XPS bands in the effects of a n-TiO_2 gate regulates (011) VO_2 bonding on a (100) Si(p^{++}) substrate in thin films.

E_b value (eV)	Core-levels	I_p	Δw (eV)	ΔE_b (eV)	Species
1. VO_2@Si(p^{++})					
515.90	$2p_{3/2}$	43	1.85	7.56	$3d^1$:V^{4+}
523.46	$2p_{1/2}$	24	2.46		
517.16	$2p_{3/2}$	21	2.10	7.80	$3d^0$:V^{5+}
524.96	$2p_{1/2}$	04	1.86		
529.75	$1s_{1/2}$	85	1.23	2.81	O^{2-}-V^{4+}
532.56	$1s_{1/2*}$	26	2.35		O^{2-}-V^{5+}
2. VO_2@TiO_2/Si(p^{++})					
515.68	$2p_{3/2}$	50	2.10	7.53	$3d^1$:V^{4+}
523.21	$2p_{1/2}$	20	3.31		
517.10	$2p_{3/2}$	28	1.92	7.95	$3d^0$:V^{5+}
525.05	$2p_{1/2}$	04	1.50		
529.47	$1s_{1/2}$	100	2.91	1.72	O^{2-}-V^{4+}
531.19	$1s_{1/2*}$	29	1.51		O^{2-}-V^{5+}

The E_b, I_p and Δw values are reported at deconvoluted bands after subtracting the background intensity. I_p: Normalized relative to a maximum 100 value in the most intense band in sample 2.

4.2.3 I-V Characteristics in Field-Induced VO_2 Metallic States

A model circuit diagram in **Figure 4.6 (a)** describes a bistable bi-local active memristor (BBAM) is made with a negative conductance 'G' put parallel to an active memristor (AM). It very efficiently controls, regulates and monitors an induced current I_m flow through two terminals of the memristor (M) at an applied field V_m in an in-plane device. As sketched in **Figure 4.6 (b)**, a device is made at two identical Al-electrodes pivoted on a film VO_2 with help of a thermal evaporator.

To feed and vary the field, a power supply is interfaced through a voltmeter (V) so to the induced I_m flows across the electrodes. Here, the effective resistance (ρ_e) of the device does not depend merely on applied fields, but rather on its hysterics in field induced charges order at the itinerant metallic states [7, 36]. In order to examine an inbuilt nanogate regulates the charge order, we measured the minor I-V loops at a first half-cycle of the sweeping field, which is varied in small steps of $0 \rightarrow 5$ V, $0 \rightarrow 10$ V, $0 \rightarrow 20$ V and $0 \rightarrow 30$ V, respectively. So, each minor loop is measured by raising-decreasing the field form '0' to a fixed value in a cycle. As the results, a low-field BBAM device made with an inbuilt nanogate SiO_2/TiO_2 in temperature. An inbuilt anisotropic electric field (E_1) controls the underlying effects of the charge order in the single VO_2 electric domains (SEDs). So, an oval-shaped I-V loop is obtained in **Figure 4.6 (c)** for the VO_2@Si films when no any gate is used. The minor loop not only spans over applied fields but also rotates (at an angle $\varphi = 27° \rightarrow 18°$) towards the final 'I' value. It is because the 'E_1' controls the SEDs (dipoles) rotate gradually along the final 'I' value in the VO_2 metallic states of 'conductive' network channels. Using an inbuilt nanogate SiO_2, an order of 'I' value is enhanced in similar loops in **Figure 4.6 (d)**, wherein φ is rotated $12° \rightarrow 29°$ more effectively in lieu of rather softened 'E_1' in co-planar (and thinner) VO_2 nanoplates

aligned along the films (according to the FESEM images in **Figure 4.4 (b)**). As SiO_2 is replaced by TiO_2 of an inbuilt nanogate, the I-V loop is turned up vertical with a wider shape over 'V' in **Figure 4.6 (e)**, as the $M_1 \rightarrow M_2$-VO_2 itinerant metallic states (shown in the XPS bands) become active at the $V^{4+} \rightarrow V^{5+} + e^-$ charges across the nanogate. The loop, which is setup along the I-axis (E_1) at $\varphi = 7°$ in the initial, ≤ 5 V, is gradually rotated away at larger V, and set up $\perp$ to the I-axis at ≥ 20 V. So, the anisotropy field 'E_1' acts primarily along c-axis and it turns down towards the in-plane (110) anisotropy at applied fields. It forms a clockwise 'memristive switching' rather than an anti-clockwise switching as shown in the other films. The BBAM stores charge in 'mini' capacitors in the forms of minor I-V loops, as shown in **Figure 4.6 (f)** over $0 \rightarrow 30$ V applied fields, which largely depends at an inbuilt nanogate, as used of SiO_2/TiO_2 over here in the VO_2@Si films. No any residual inductive and capacitive charge, $I \rightarrow 0$ at $V \rightarrow 0$, persists as soon as the field is turned off in a reversible charge-discharge cycle. As usual [36, 7], a due energy is stored up to the charge-storing capacity in the SEDs at only charge $\leftrightarrow$ discharge fields.

Table 4.3 The effects of a nano SiO_2/TiO_2 gate on energy stored in the hysteresis I-V loops in the VO_2 films gown at a Si(p^{++}) substrate.

Films / Voltage	Energy (J/s)				V_t (V)
	5 V	10 V	20 V	30 V	
VO_2@Si	2.96×10^{-5}	9.11×10^{-5}	31.50×10^{-5}	71.70×10^{-5}	5.0
VO_2@SiO_2/Si	1.92×10^{-5}	9.82×10^{-5}	78.01×10^{-5}	0.002	0.13
VO_2@TiO_2/Si	10.59×10^{-5}	32.04×10^{-5}	71.70×10^{-5}	0.001	0.12

The values are reported at RT.

The energies stored in the 'mini' capacitors in selected charge ↔ discharge cycles are given in **Table 4.3** for the three different BBAM devices made of VO_2@Si, VO_2@SiO_2-Si, and VO_2@TiO_2-Si films. Thus, a maximum value 0.002 J/s is stored in the VO_2@SiO_2-Si device, but at rather high fields, 0 ↔ 30 V, as used here.

Nevertheless, SiO_2 - a low dielectric (k) phase is not so suitable for portable electronics [19]. At rather low fields, ≤ 20 V, a reasonably better power, ≤ 0.7 nW, is achieved when an n-TiO_2 nanogate is sued in the VO_2@Si films. The TiO_2 (a high-k phase [17]) promptly regulates a well-controlled Vt → 0.12 V, useful for operating low field devices at ≤ 1.0 V [17–19]. It duly controls the leakage current (at a moderate 'I' in the I-V curves) at reduced trap states at the VO_2-TiO_2 interfaces on an electronic (100) Si(p^{++}) substrate.

Presumably, duly varied $V^{4+} \rightarrow V^{3+}/V^{5+}$ charge states fill up the interface 'trap states' so that streamline a duly high performance at desirably low fields. As a result, a charge regulated 'I' flows in the field induced streamlined $M_1/M_2 \rightarrow R_1$/R-VO_2 conductive metallic states. In general, a value, ρ_e = V/I persist in response to an applied field and the field induced charges order in 'conductive' metallic states in a pool of recurring charge carriers. As portrayed in **Figure 4.7 (a)** for a BBAM of the VO_2@Si films, an induced ρ_e at 0 → 30 V fields arises up in a parabolic path up to its vertex (lies at a critical value V_t = 5 → 15 V) before it starts decreasing after a saturation on its longer trajectory. At decreasing V → 0 in an ON/OFF scheme, a modulated ρ_e follows a revived path (given in the inset) in a loop in a reversible cycle. At a nanogate SiO_2 in the VO_2@SiO_2-Si films, a sharp V_t peak is peaked up at a very low field 0.13 V in **Figure 4.7 (b)** in a 0 ↔ 5 V low field switch. It is shifted further at 0.12 V as the SiO_2 is replaced by TiO_2 in the VO_2@TiO_2-Si films in **Figure 4.7 (c)**. It is the smallest value reported so far for low field, ≤ 1.0 V, devices [10, 19].

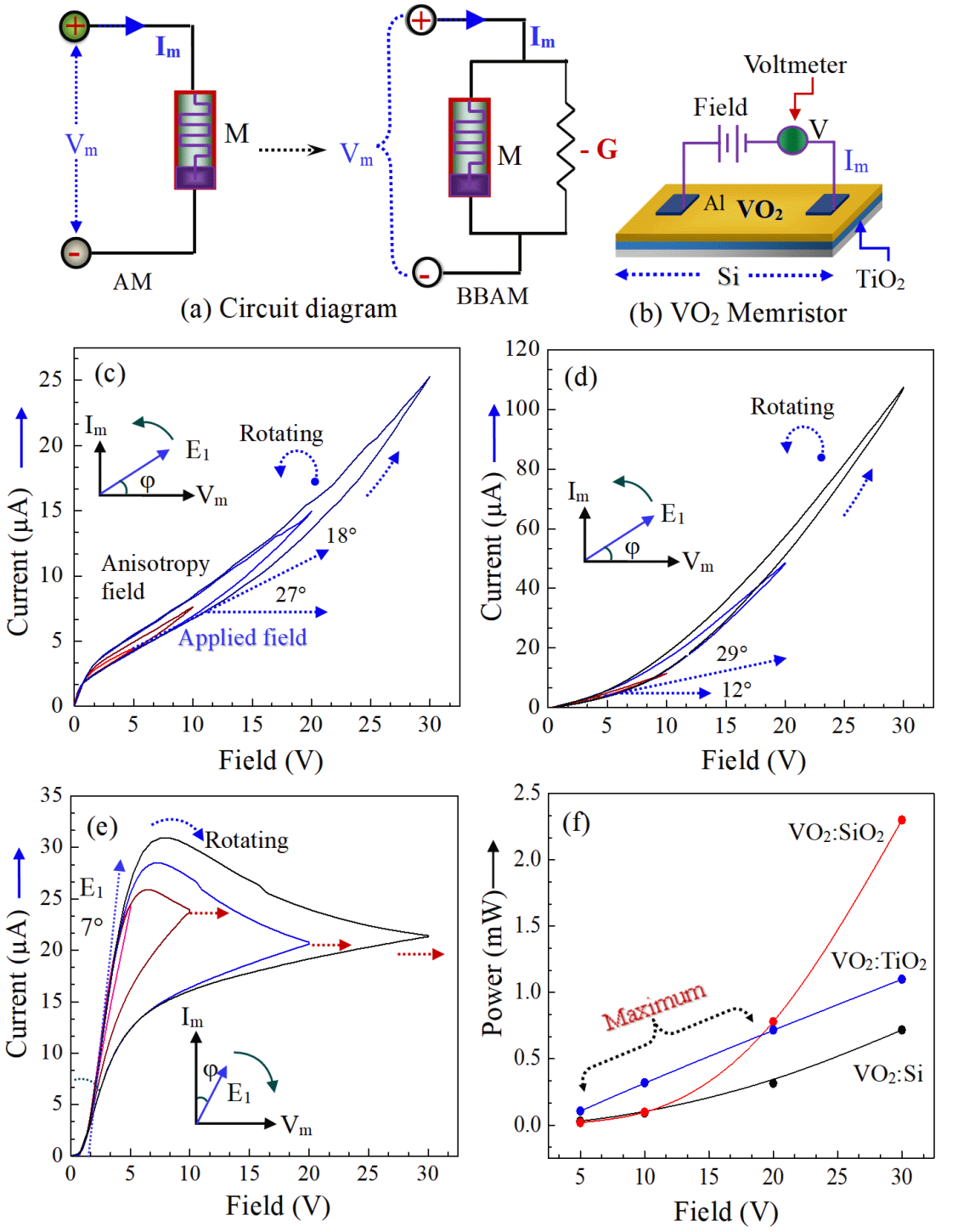

Figure 4.6 (a) Schematics of an AM and a BBAM, (b) a typical VO_2@TiO_2-Si memristor, and I-V plots for the films VO_2 grown at (100) Si (c) before and after a nano-gate (d) SiO_2 and TiO_2, and (f) power outputs regulated at the films at different fields.

At larger swiping fields, such as 0-10 V, 0-20 V and 0-30 V in the ON/OFF schemes, a revived V_t assumes successively larger values 0.31 V, 0.51 V and 0.81 V in the VO_2@SiO_2-Si films, while 0.25 V, 0.50 V and 0.74 V, respectively, in the VO_2@TiO_2-Si films. It anticipates a synergistic effect of the field induced exotic charges order in the metallic VO_2 states across the nanogate used.

At a low field 0 → 5 V switch, two distinct V_t peaks are noticed at 0.25 V and 0.42 V in two major types of $V^{4+} \rightarrow V^{5+}$ charges co-exist at the VO_2-TiO_2 interfaces. They are merged each other at larger fields.

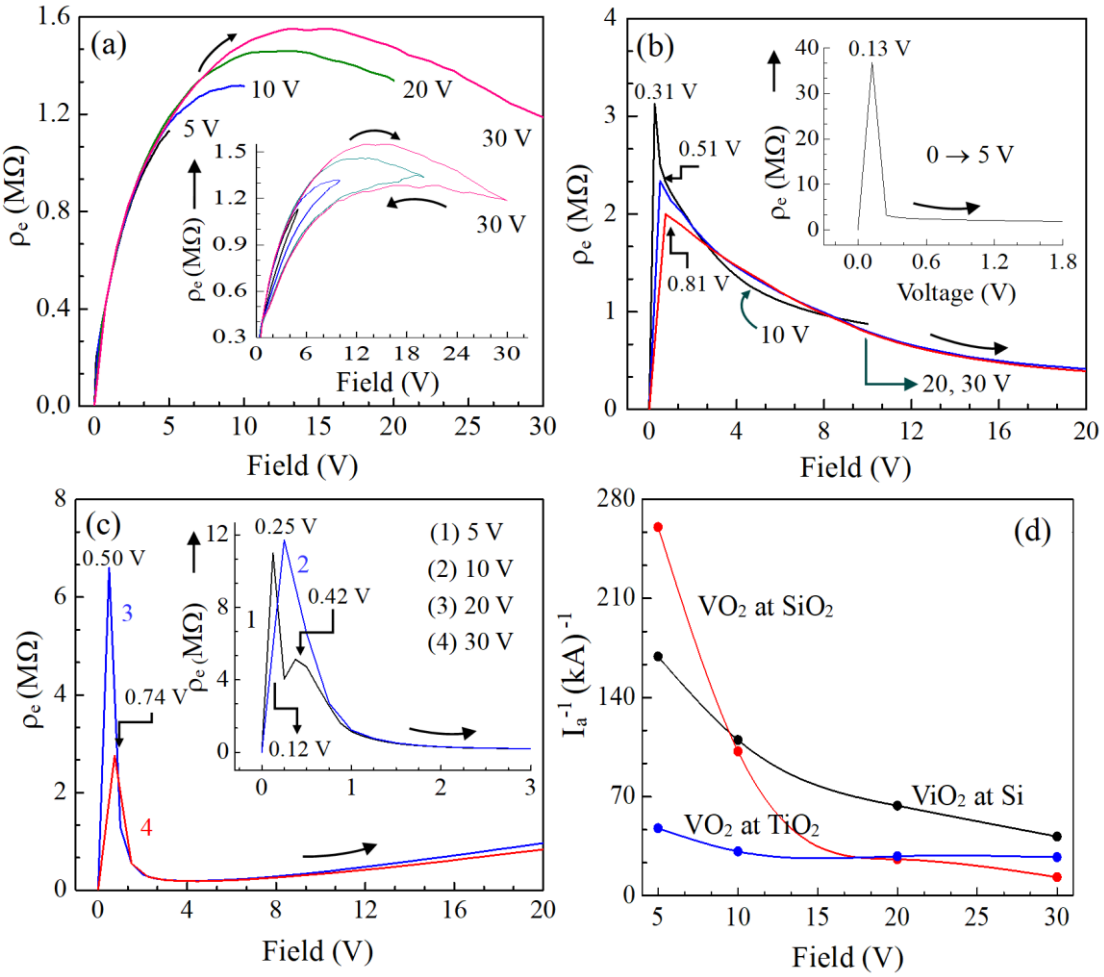

Figure 4.7 Modulated (a, b, c) resistance (ρ_e) and (d) reciprocal of current (I_e^{-1}) measured at an increasing voltage (towards arrows) for thin VO_2 films grown at (a) Si, (b) SiO_2 and (c) TiO_2.

Further, a mean $<\rho_e>$ per unit volt is derived from the integrated area in the minor I-V loops scanned over specific swiping fields, as $<\rho_e>/V \cong (IV/V)^{-1} \cong I_a^{-1}$.

It is a nontrivial stimulus to probe the $<\rho_e>$ nonlinearity in terms of I_a^{-1} as a function of V, as plotted in **Figure 4.7 (d)**. Practically, it is well stabilized over 5 → 30 V at a high-k TiO_2 nanogate efficiently controls over the leakage current. It is rapidly dropped by an order of magnitude at low swiping fields, ≤ 15 V, when a low-k SiO_2 is used in the VO_2@SiO_2-Si films.

4.3 Conclusion

A nanogate SiO_2/TiO_2 is inbuilt to tune the interface VO_2 bonding, crystal structure, and functional properties. A low-field memristor device is made from the VO_2 films to operate it in an ON/OFF switching mode in a prototype two-terminal device. The roles of a nanogate SiO_2/TiO_2 in charge transfer in the VO_2@(100) Si(p^{++}) films is studied in which a high-k TiO_2 efficiently controls and regulates field-induced output in a reversible I-V loop (current-voltage). In a low field 0 ↔ 5 V swipe, a V_{th} as small as V_t = 0.12 V is achieved in a sharp peak. At wider swiping fields, such as 0 → 10, 20, and 30 V, it is shifted successively at 0.25, 0.50, or 0.74 V, in the field-induced charges order across the gate. An ion exchange, V^{3+}-e^- ← V^{4+} → V^{5+}+e^- , in a pool, leads to streamline conduction in 'conductive through channels' in the itinerant M_1 → $M_2/R_1/R_2$/R-VO_2 metallic states. Thus, a smaller V_t lasts than ever reported before at low field, ≤ 1.0 V, devices [10, 19]; especially fast ON/OFF switches, logic gates, informatics, neurology, and many others. The results have a wide scope of developing the charge dynamics as well as the technology of VO_2-type metal oxide SCs.

REFRENCES

[1] L. Pellegrino, N. Manca, T. Kanki, H. Tanaka, M. Biasotti, E. Bellingeri, A. S. Siri, and D. Marré, "Multistate Memory Devices Based on Free-Standing VO_2/TiO_2 Microstructures Driven by Joule Self-Heating," *Advanced Materials*, **24** (2012) 2929–2934.

[2] S. H. Bae, S. Lee, H. Koo, L. Lin, B. H. Jo, C. Park, and Z. L. Wang, "The Memristive Properties of a Single VO_2 Nanowire with Switching Controlled by Self-Heating," *Advanced Materials*, **25** (2013) 5098–5103.

[3] I. A. Mogunov, S. Lysenko, A. E. Fedianin, F. E. Fernández, A. Rúa, A. J. Kent, A. V. Akimov, and A. M. Kalashnikova, "Large Non-Thermal Contribution to Picosecond Strain Pulse Generation Using the Photo-Induced Phase Transition in VO_2," *Nature Communication*s, **11** (2020) 1690 (8).

[4] J. Tadeo, D. Bhardwaj, D. Sheela, S. B. Krupanidhi, and A. M. Umarji, "Highly Photoresponsive VO_2 (M_1) Thin Films Synthesized by Dc Reactive Sputtering," *Journal of Materials Science: Materials in Electronics*, **31** (2020) 4687–4695.

[5] Z. Chen, Q. Y. Wen, K. Dong, D. D. Sun, D. H. Qiu, and H. W. Zhang, "Ultrafast and Broadband Terahertz Switching Based on Photo-Induced Phase Transition in Vanadium Dioxide Films," *Chinese Physics Letters*, **30** (2013) 017102 (4).

[6] A. G. Shabalin, E. Anouchi, N. Hua, Y. A. Wu, M. V. Holt, A. Sharoni, and O. G. Shpyrko, "Twinned Nanostructure of VO_2 Thin Films Grown on R-Cut Sapphire," *Physical Review B*, **102** (2020) 134106 (7).

[7] T. Driscoll, H. T. Kim, B. G. Chae, M. D. Ventra, and D. N. Basov, "Phase Transition Driven Memristive System," *Applied Physics Letters*, **95** (2009) 043503 (3).

[8] Z. Yang, C. Ko, and S. Ramanathan, "Metal-Insulator Transition Characteristics of VO_2 Thin Films Grown on Ge (100) Single Crystals," *Journal of Applied Physics*, **108** (2010) 073708 (6).

[9] M. Seo, J. Kyoung, H. Park, S. Koo, H. S. Kim, H. Bernien, B. J. Kim, J. H. Choe, Y. H. Ahn, H. T. Kim, N. Park, Q. H. Park, K. Ahn, and D. S. Kim, "Active Terahertz Nanoantennas Based on VO_2 Phase Transition," *Nano Letters*, **10** (2010) 2064–2068.

[10] R. Naik, B. D. Verma, and V. Balakrishnana, "Effect of Chemical Doping on Memristive Behaviour of VO_2 Microcrystals," *Applied Physics Letters*, **120** (2022) 062101 (6).

[11] B. Hong, K. Hu, Z. Tao, J. Zhao, N. Pan, X. Wang, M. Lu, Y. Yang, Z. Luo, and C. Gao, "Polymorph Separation Induced by Angle Distortion and Electron

Delocalization Effect via Orbital Modification in VO_2 Epitaxial Thin Films," *Physical Review B*, **95** (2017) 075433 (9).

[12] S. Majid, D. K. Shukla, F. Rahman, S. Khan, K. Gautam, A. Ahad, S. Francoual, R. J. Choudhary, V. G. Sathe, and J. Strempfer, Insulator-Metal Transitions in the *T* phase Cr-Doped and *M*1 Phase Undoped VO_2 Thin Films," *Physical Review B*, **98** (2018) 075152 (9).

[13] J. Y. Suh, R. Lopez, L. C. Feldman, and R. F. Haglund, "Semiconductor to Metal Phase Transition in the Nucleation and Growth of VO_2 Nanoparticles and Thin Films," *Journal of Applied Physics*, **96** (2004) 1209–1213.

[14] Y. Zhou, X. Chen, C. Ko, Z. Yang, C. Mouli, and S. Ramanathan, "Voltage-Triggered Ultrafast Phase Transition in Vanadium Dioxide Switches," *IEEE Electron Device Letters*, **34** (2013) 220–222.

[15] J. Lin, H. Ji, M. W. Swift, W. J. Hardy, Z. Peng, X. Fan, A. H. Nevidomskyy, J. M. Tour, and D. Natelson, "Hydrogen Diffusion and Stabilization in Single-Crystal VO_2 Micro/Nanobeams by Direct Atomic Hydrogenation," *Nano Letters*, **14** (2014) 5445–5451.

[16] Z. Tian, B. Xu, B. Hsu, L. Stan, Z. Yang, and Y. F. Mei, "Reconfigurable Vanadium Dioxide Nanomembranes and Microtubes with Controllable Phase Transition Temperatures," *Nano Letters*, **18** (2018) 3017–3023.

[17] S. Sung, S. Park, W. J. Lee, J. Son, C. H. Kim, Y. Kim, D. Y. Noh, and M. H. Yoon, "Low-Voltage Flexible Organic Electronics Based on High-Performance Sol-Gel Titanium Dioxide Dielectric," *ACS Applied Materials and Interfaces*, **7** (2015) 7456–7461.

[18] N. Shukla, A. V. Thathachary, A. Agrawal, H. Paik, A. Aziz, D. G. Schlom, S. K. Gupta, R. E. Herbert, and S. Datta, "A Steep-Slope Transistor Based on Abrupt Electronic Phase Transition," *Nature Communications*, **6** (2015) 7812 (6).

[19] A. Sharma, N. K. Chourasia, N. Pal, S. Biring, and B. N. Pal, "Role of Electron Donation of Tio_2 Gate Interface for Developing Solution-Processed High Performance One-Volt Metal-Oxide Thin-Film Transistor Using Ion-Conducting Gate Dielectric," *Journal of Physical Chemistry C*, **123** (2019) 20278–20286.

[20] L. Chua, "Memristor-the Missing Circuit Element," *IEEE Transactions on Circuit Theory*, **18** (1971) 507–519.

[21] P. Markov, R. E. Marvel, H. J. Conley, K. J. Miller, R. F. Haglund Jr., and S. M. Weiss, "Optically Monitored Electrical Switching in VO_2," *ACS Photonics*, **2** (2015) 1175–1182.

[22] H. Yu, A. N. M. N. Islam, S. Mondal, A. Sengupta, and S. Ramanathan, "Switching Dynamics in Vanadium Dioxide-Based Stochastic Thermal Neurons," *IEEE Transactions on Electron Devices*, 69 (2022) 3135–3141.

[23] M. Pattanayak, M. N. F. Hoque, Y. C. Ho, W. Li, Z. Fan, and A. A. Bernussi, "Ultrahigh Tunability of Resistive Switching in Strongly Correlated Functional Oxide," *Applied Materials Today*, **30** (2023) 101642 (11).

[24] A. Rana, C. Li, G. Koster, and H. Hilgenkamp, "Resistive Switching Studies in VO_2 Thin Films," *Scientific Report*, **10** (2022) 3293 (6).

[25] X. Sun, Z. Qu, J. Yuan, E. Cheng, P. Wang, and Q. Wang, "Voltage-Induced Phase Transition of VO_2@SiO_2 Nanoparticles," *Ceramic International*, **47** (2021) 29011–29022.

[26] Y. Gao, S. Wang, H. Luo, L. Dai, C. Cao, Y. Liu, Z. Chen, and M. Kanehira, "Enhanced Chemical Stability of VO_2 Nanoparticles by the Formation of SiO_2/VO_2 Core/Shell Structures and the Application to Transparent and Flexible VO_2-Based Composite Foils with Excellent Thermochromic Properties for Solar Heat Control," *Energy and Environmental Science*, **5** (2012) 6104–6110.

[27] X-Ray Powder Diffraction JCPDS Files, (a) 01-082-661; Monoclinic VO_2 and (b) 01-079-1655; Rutile VO_2, Joint Committee on Powder Diffraction Standard International Centre for Diffraction Data, Swarthmore, PA, USA, 2019.

[28] P. V. Rajeswari, S. K. Sharma, S. Ram, and D. Pradhan, "Nanoporous N/O:Sp^2-C Films Functionalized at Nonbonding Electrons of a Biogenic Husk (Green Chili) with Deep UV-Visible Light Absorption-Emission for Photocatalysis and other Applications," *Surfaces and Interfaces*, **38** (2023) 102824 (20).

[29] J. Du, Y. Gao, H. Luo, L. Kang, Z. Zhang, Z. Chen, and C. Cao, "Significant Changes in Phase-Transition Hysteresis for Ti-Doped VO_2 Films Prepared by Polymer-Assisted Deposition," *Solar Energy Materials and Solar Cells*, **95** (2011) 469–475.

[30] C. Zhang, W. Cao, A. V. Adedeji, and H. E. Elsayed-Ali, "Preparation and Properties of VO_2 Thin Films by a Novel Sol-Gel Process," *Journal of Sol-Gel Science and Technology*, **69** (2014) 320–324.

[31] G. Y. Song, C. Oh, S. Sinha, J. Son, and J. Heo, "Facile Phase Control of Multivalent Vanadium Oxide Thin Films (V_2O_5 and VO_2) by Atomic Layer Deposition and Postdeposition Annealing," *ACS Applied Materials and Interfaces*, **9** (2017) 23909–23917.

[32] G. K. Williamson, and W. H. Hall, "X-Ray Line Broadening from Filed Aluminium and Wolfram," *Acta Metallurgica*, **1** (1953) 22–31.

[33] M. Tahir, "Hierarchical 3D VO_2/ZnV_2O_4 Microspheres as an Excellent Visible Light Photocatalyst for CO_2 Reduction to Solar Fuels," *Applied Surface Science*, **467–468** (2019) 1170–1180.

[34] Y. Jung, H. Han, A. Sharma, J. Jeong, S. S. P. Parkin, and J. K. S. Poon, "Integrated Hybrid VO_2-silicon Optical Memory," *ACS Photonics*, **9** (2022) 217−223.

[35] P. V. Rajeswari, B. Tiwari, S. Ram, and D. Pradhan, "A Biogenic TiO_2-C-O Nanohybrid Grown from a Ti^{4+}-Polymer Complex in Green Tissues of Chilis, Interface Bonding, and Tailored Photocatalytic Properties," *Journal of Materials Science*, **53** (2018) 3131–3148.

[36] Z. Yang, C. Ko, and S. Ramanathan, "Oxide Electronics Utilizing Ultrafast Metal-Insulator Transitions," *Annual Review of Materials Research*, **41** (2011) 337−367.